geosciences

MDPI

Article

Investigation of the Effect of Integrated Offset, GPS, and InSAR Data in the Stochastic Source Modeling of the 2002 Denali Earthquake

Parva Shoaeifar [1,*] and Katsuichiro Goda [1,2]

[1] Department of Earth Sciences, University of Western Ontario, London, ON N6A 5B7, Canada; kgoda2@uwo.ca
[2] Department of Statistical & Actuarial Sciences, University of Western Ontario, London, ON N6A 5B7, Canada
* Correspondence: pshoaeif@uwo.ca

Abstract: This study investigates the effect of geological field measurement (offset), global positioning system (GPS), and interferometric synthetic aperture radar (InSAR) data on the estimation of the co-seismic earthquake displacements of the 2002 Denali earthquake. The analysis is conducted using stochastic source modeling. Uncertainties associated with each dataset limit their effectiveness in source model selection and raise questions about the adequate number of datasets and their type for reliable source estimation. To address these questions, stochastic source models with heterogeneous earthquake slip distributions are synthesized using the von Kármán wavenumber spectrum and statistical scaling relationships. The surface displacements of the generated stochastic sources are obtained using the Okada method. The surface displacements are compared with the available datasets (i.e., offset, GPS, and InSAR) individually and in an integrated form. The results indicate that the performance of stochastic source generation can be significantly improved in the case of using GPS data and in the integrated case. Overall, based on the case study of the 2002 Denali earthquake, the combined use of all available datasets increases the robustness of the stochastic source modeling method in characterizing surface displacement. However, GPS data contribute more than InSAR and offset data in producing reliable source models.

Keywords: stochastic source modeling; 2002 Denali earthquake; Okada equations; co-seismic surface displacement

Citation: Shoaeifar, P.; Goda, K. Investigation of the Effect of Integrated Offset, GPS, and InSAR Data in the Stochastic Source Modeling of the 2002 Denali Earthquake. *Geosciences* **2024**, *14*, 300. https://doi.org/10.3390/geosciences14110300

Academic Editors: Claudia Pirrotta and Maria Serafina Barbano

Received: 20 August 2024
Revised: 31 October 2024
Accepted: 5 November 2024
Published: 6 November 2024

1. Introduction

Fault displacement hazard analysis is critically important in structural design and in increasing the seismic resistance and reliability of structures against earthquake displacements. Many critical infrastructures, such as bridges, tunnels, dams, railways, roads/highways, and pipelines, could be damaged during large earthquakes due to surface displacements. Investigating the surface displacement hazard caused by earthquakes is essential for the financial risk assessment of physical damage, interruption of utility services, and social and environmental problems [1–5]. Hence, ground displacement hazards should be taken into consideration as a critical issue.

In this regard, many researchers have worked on this problem over the years and proposed methodologies for fault displacement hazard assessment [6–12]. These methodologies are based on empirical predictive relationships between the earthquake magnitude and various spatial dimensions of the earthquake, such as the along-strike length, down-dip width, rupture area, and peak and mean slip of on-fault and off-fault surface ruptures [8,13–17]. The empirical predictive relationships are often defined by seismological criteria, such as aftershock distributions and finite fault models [15,18–24]. Although these geologically derived slip distributions are widely used to establish fault rupture information from sparse offset measurements, they may contain biases. For instance, the distribution of aftershocks may

not represent the true rupture area [25,26], or the product of the fault length and width may overestimate the rupture area. In addition, non-unique inverse solutions of earthquakes result in multiple possible source models that are not accounted for in a single-solution approach. Furthermore, the inversion of observations for the spatial characteristics of earthquakes can lead to unstable or highly regularized source inversions [27–29]. This is due to the fact that regularization controls the trade-off between the fit to the data and solution stability. Regarding the limitations of empirical relationships, a methodology for stochastic source-based PFDHA [30] offers an alternative way to characterize the fault displacement hazard. In this regard, the available geological and geodetic data are utilized to select the source models representing the realistic approximation of the earthquake displacement.

Many studies have examined the source process of the Denali earthquake using different datasets [31–39]. One of the main challenges in earthquake source characterization is selecting datasets and data correction. Data correction includes comparing datasets and eliminating measurements with high uncertainty that poorly match with other sources or identifying duplicate measurements or missing data [40]. The challenge of selecting datasets for source inversion is due to the complex nature of earthquakes, the availability and quality of the datasets, and the geological, geophysical, and geographical conditions.

The aim of this study is to investigate the adequacy of different datasets to characterize reliable rupture models by using a stochastic source modeling approach and applying the method to the 2002 Denali earthquake with a moment magnitude (Mw) of 7.9. The Denali earthquake was a shallow crustal earthquake that caused significant surface ruptures and the failure of linear structures crossing the ruptured zones. The Trans-Alaska Pipeline System was designed to accommodate the surface displacements of the Denali fault crossing the route of the pipeline [41]. As a great technological achievement, the pipeline survived the earthquake as the result of seismotectonic studies and field surveys by engineers in the 1970s [42]. Thus, studying the surface displacement of this earthquake can contribute to better risk assessments of structures and infrastructure exposed to large crustal earthquakes.

In the following sections, surface displacement results generated by simulated source models for the 2002 Denali earthquake are presented. We compare the estimated displacement results with field offset measurements, GPS, and InSAR data, as well as the existing benchmark studies. The findings address the question of whether the integrated use of ground truth and remotely sensed data can leverage the performance of stochastic source modeling or not.

2. Seismotectonic Setting

The Denali fault system, with a right-lateral strike-slip mechanism, extends for hundreds of kilometers across Alaska [43]. An Mw 6.7 strike-slip foreshock struck Central Alaska on 23 October 2002, followed by the Mw 7.9 earthquake 11 days later. The mainshock was triggered in a relatively small thrust segment, which was northeast-striking. Subsequently, it continued onto the central Denali fault, which was a right-lateral strike-slip, for about 220 km. Finally, the rupture was transferred to the Totschunda fault and terminated after approximately 80 km. Figure 1 shows five segments of the ruptured faults, consisting of the north-dipping Susitna Glaciers fault at the west end with a thrusting mechanism, the strike-slip central Denali faults in the middle, and the strike-slip Totschunda junction at the eastern end of the fault system.

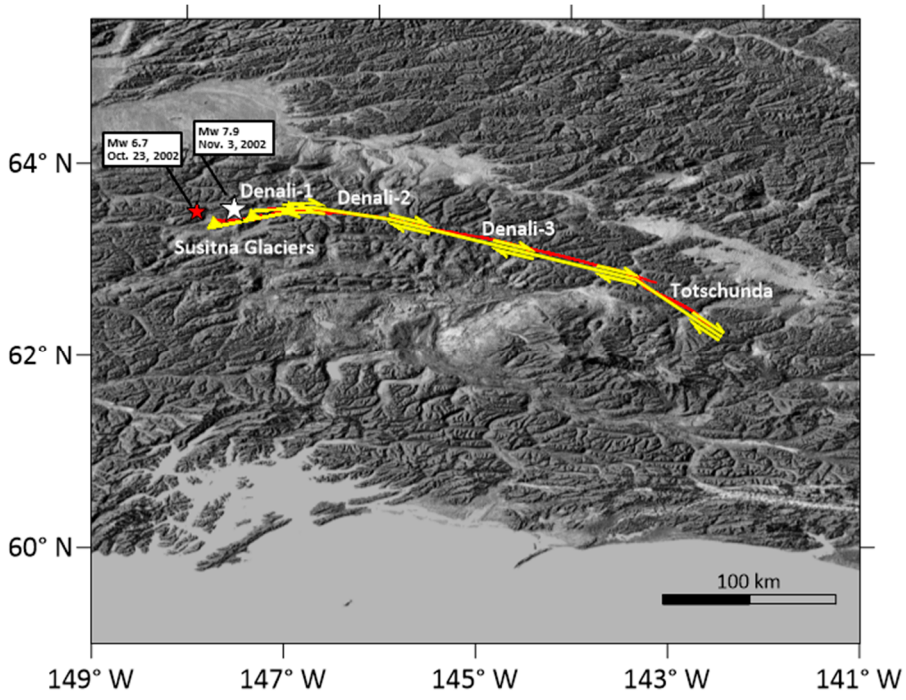

Figure 1. Surface projection of the 2002 Denali earthquake fault model (yellow lines) shown on the shaded relief map of Alaska. The Denali 1 to 3 and Totschunda faults are indicated by arrows, and the Susitna Glaciers thrust fault is shown with barbs on the hanging wall. The red lines indicate mapped surface ruptures [44]. The epicenter and magnitude data are taken from the USGS.

3. Data and Stochastic Source Modeling of the 2002 Denali Earthquake

A retrospective hazard analysis starts with the model evaluation of benchmark studies, which will be detailed in the final part of this section, and data collection. The adopted datasets for the Denali earthquake analysis, as well as the associated uncertainties, are elaborated in the subsequent section.

3.1. Dataset Adopted in This Study

In the present study, three datasets are used: horizontal and vertical surface offsets reported by the Denali Fault Earthquake Field Geology Team [42,45], horizontal and vertical displacements measured by continuous and campaign-mode static GPS stations [38,39], and line-of-sight (LOS) displacement measurements of InSAR satellite monitoring ([34]; interferograms were provided by Dr. Wright).

Offset data are available for the near-fault region along the ruptured fault in two components (horizontal and vertical components). The average recorded surface offsets along the Denali fault were 4.5–5.1 m with a maximum of 8.8 m [45]. Nevertheless, the sources of uncertainty were inevitable, especially in the case of field investigations. The uncertainties associated with the collected offset data included gaps in data points, measurement uncertainty, the presence of glacier areas, slip steps, and changes in slip values over short distances [45]. Due to the complex nature of the rupture, small offset fractures diverged from the fault trace, particularly in the areas covered with glacier ice or landslide debris. The presence of these small fractures limited the possibility of identifying features for measurements along the fault trace and decreased the number of measurements. Furthermore, the measurements of the features crossing the fault trace had uncertainties corresponding to the unclear geometry of the ruptured feature prior to its offset. Such uncertainty increases in glacier areas, where glacier ice often lowers the measurements of the total slip. For instance, the offset measurements of 59 km and 62.5 km east of the epicenter located in glacier ice were eliminated from the collected data due to the underestimation of the total slip [45]. Furthermore, the spatial variability of the slips within the transfer zones of the

deformation field (e.g., Denali–Toschunda transfer zone) was high. Finally, there were some areas with abrupt changes in slip values within short distances. Although there is no clear reason, geometrical factors and the localized complexities of the fault structure can contribute to such spatially frequent variations.

GPS data are more widely distributed in comparison with offset and InSAR data. GPS data comprise two horizontal components and a vertical component of the deformation field, and they are available in areas with no InSAR coverage (i.e., the eastern part of the Denali fault). The number of high-precision GPS measurements in Alaska was limited prior to the 2002 Denali earthquake, and the distribution of all available sites was not optimal [38,46]. Hreinsdóttir et al. [38] presented 40 GPS datasets for the Denali earthquake. Hreinsdóttir et al. [39] added GPS data from highway surveys (along the Richardson Highway) to the fault trace and estimated the co-seismic displacements of 232 GPS stations within 350 km of the earthquake rupture. The recording stations comprised 180 campaign stations and 12 permanent stations. The dataset was consistent with the offset data from a large-scale view, but there were some inconsistencies in details, especially for the Susitna Glacier and Totschunda segments of the rupture, in which the coverage of GPS stations was poor. Apart from the limited spatial coverage, there was a lack of adequate GPS data on the Susitna Glacier segment, which required reliance on other datasets to resolve the shallow slip distribution. Another limitation of the GPS data was uncertainty due to local effects, such as liquefaction and landslides. Hence, the measurements with high uncertainty were excluded from the recorded GPS data [39]. One of the other challenges associated with the GPS data was the temporal gap corresponding to the collection of data prior to the earthquake [39]. While GPS data provide valuable information about ground deformation, they may not cover the full complexity of the earthquake displacement.

Lastly, InSAR data are collected in the line-of-sight direction of the satellite. In the case of the 2002 Denali earthquake, there are challenges associated with InSAR data. There are SAR images of the Radarsat-1 satellite available in the Alaska SAR Facility for the western end of the Denali fault (i.e., Susitna Glaciers segment). However, there are no SAR data for the eastern part of the fault [47]. For the ruptured area of the Susitna Glaciers segment, in which InSAR data are available, forming a coherent interferogram is challenging due to the presence of snow and glaciers. These limitations can significantly constrain the efficiency of InSAR data in mapping surface deformations and highlight the important role of integrated data sources in accurately modeling the surface displacement of earthquakes. Overall, it is important to characterize the co-seismic surface displacement based on the collection of independent displacement measurements to constrain the source models and have a reliable three-dimensional displacement field solution [48].

3.2. Source Modeling of the 2002 Denali Earthquake

The next step of the analysis is generating stochastic source models. It includes setting an arbitrary simulation number, determining the magnitude of the earthquake, and subsequently characterizing the methodology for the stochastic source modeling. The simulation number can be changed later based on the stability of the results, and the magnitude of the earthquake can be retrieved from previous studies. The stochastic source modeling approach is based on the simulation of the earthquake rupture characteristics using statistical methods [30], and the surface displacement calculation is based on the Okada [49] equations. The Okada equations evaluate the three translational surface fault displacements with the assumption of a uniform half-space and elastic material behavior. The surface deformation of the generated sources is compared with the surface deformation of existing studies based on the available data (i.e., offset, GPS, and InSAR data), and models that closely match the observations are selected. Furthermore, the source models with the best match with individual datasets are provided to evaluate the effect of each dataset on the stochastic source model selection. The stochastic source modeling method is elaborated for the Denali earthquake in the following; more information can be found in [30]. The first step of stochastic source modeling is specifying the (multiple) fault plane

geometry and earthquake scenario. Subsequently, statistical scaling relationships of the source parameters (i.e., fault length (L), fault width (W), mean slip (Da), maximum slip (Dm), Box–Cox parameter (λ_{BC}), along-strike correlation length (CL_L), along-dip correlation length (CL_W), and Hurst number (H)) are employed based on [50]. Source parameters are estimated through Fourier spectral analysis. The fault length and width represent the geometry of the source, while the mean and maximum slip and Box–Cox parameters indicate the marginal slip distribution along the dip and strike directions. Using the Box–Cox parameter, a positive skewness is applied to the output random field generated by the Fourier integral method. The scaling relationships of the source parameters are shown in Equation (1).

$$log_{10}X = a + bMw + c\varepsilon_X \quad (1)$$

where X represents the source parameters, and a, b, and c are the parameters of the scaling relationships. ε_X represents the correlated regression residuals of the source parameters (assumed to follow a normal distribution). λ_{BC} and H are not considered to be correlated with other source parameters. Table 1 summarizes the statistical scaling relationships of the source parameters retrieved from Table 1 of [50] for non-tsunamigenic model types. The linear correlation coefficients of the source parameters are outlined in Table 2, retrieved from Table 2 of [50]. Figure 2 shows four of the source parameters for the magnitude range of 7 to 8, along with the corresponding scaling relationships.

Table 1. Parameters of the statistical scaling relationships for strike-slip, normal, and reverse faulting mechanisms [50].

Source Parameter	***a***	***b***	***c***
Length L (km)	−2.162	0.549	0.172
Width W (km)	−0.689	0.289	0.146
Mean slip Da (m)	−4.361	0.624	0.250
Maximum slip Dm (m)	−3.739	0.615	0.225
Box–Cox parameter λ_{BC}	Normal variable with [mean = 0.312, standard deviation = 0.278]		
Along-strike correlation length CL_L (km)	−2.466	0.511	0.220
Along-dip correlation length CL_W (km)	−1.335	0.303	0.159
Hurst number H	0.99 with 43% probability/normal distribution with 57% probability and [mean = 0.714, standard deviation = 0.172]		

Table 2. Correlation coefficients of six source parameters [50].

Correlation Coefficient	ε_L	ε_L	ε_L	ε_L	ε_L	ε_L
ε_L	1.0	0.139	−0.595	−0.516	0.734	0.249
ε_W	0.139	1.0	−0.680	−0.545	0.035	0.826
ε_{Da}	−0.595	−0.680	1.0	0.835	−0.374	−0.620
ε_{Dm}	−0.516	−0.545	0.835	1.0	−0.337	−0.564
ε_{CL_L}	0.734	0.035	−0.374	−0.337	1.0	0.288
ε_{CL_W}	0.249	0.826	−0.620	−0.564	0.288	1.0

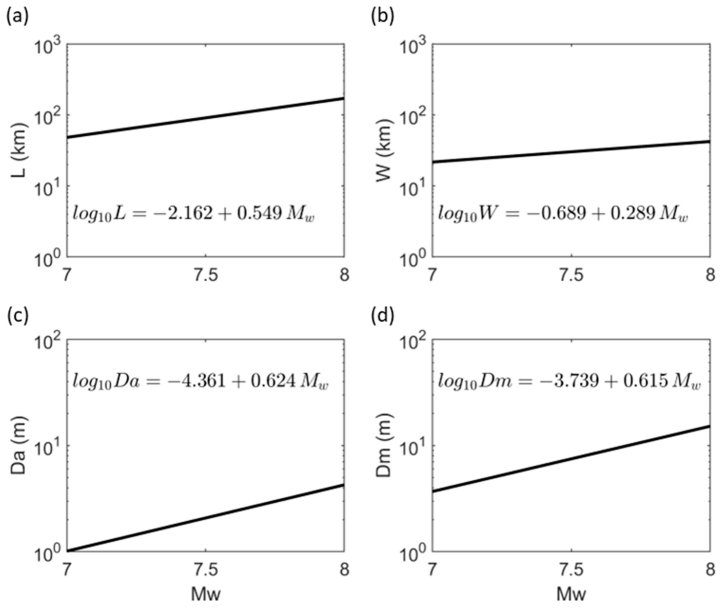

Figure 2. Stochastic source modeling parameters and scaling relationships: (**a**) fault length (*L*), (**b**) fault width (*W*), (**c**) average slip (*D*a), and (**d**) maximum slip (*D*m).

Heterogeneous earthquake slip distributions are synthesized to generate various stochastic source models. To characterize the spatial slip distribution, the von Kármán wavenumber spectrum is considered [51,52]. The corresponding parameters (i.e., the correlation lengths along the dip and strike and Hurst number) are sampled to determine the feature of the power spectrum, such as its absolute level in the low-wavenumber range and its slope in the high-wavenumber range. The mean and maximum slip values are utilized to adjust the resulting distribution. Subsequently, the corresponding seismic moment is calculated for the generated source model, maintaining consistent values of *L*, *W*, and *D*a. The stochastic source model is deemed acceptable if it produces the seismic moment within the target range (e.g., *M*w 7.8 and *M*w 8.0 in the case of the 2002 Denali earthquake). The procedure of generating potential source models continues until a desired number of accepted source models is achieved [50].

The studies of Wright et al. [34], Asano et al. [37], and Hreinsdóttir et al. [39] are selected as comprehensive benchmark inversion studies using InSAR, strong motion, and GPS data to compare with the generated source model in this study. The model parameters of the fault planes considered in the benchmark studies are shown in Table 3.

In the next step, the displacement fields of the three orthogonal directions are calculated for each source model using the Okada equations [49]. The deformation field of a finite rectangular source is calculated using Equations (1A) to (6A) of Appendix A. The surface displacements are compared with the field observations, GPS, and InSAR data. The total number of offset data utilized for the source evaluation is 107. These data are selected based on the availability of horizontal and vertical displacement components. The uncertainty in the offset measurements ranges from less than 10% to 50% [45]. In addition to the offset data, the measurements of 226 GPS stations are used for the source evaluation. Three far-away sites, together with another three sites affected by local effects (e.g., liquefaction), are excluded from the source evaluation. Regarding the InSAR data, due to the lack of SAR data (available only for the western part of the fault) and incoherency in the available data, 173 points are selected with an 8 km space in an area with about a 110 km length along the longitude and about a 150 km width along the latitude from the available interferogram. The selected points for all datasets, as well as the observed interferogram in the line-of-sight direction, are shown in Figures 3b and 4b. The values of the horizontal GPS and offset data are shown in the longitude and latitude directions in

Figure 3a,c, respectively. The values of the vertical GPS and offset data are shown in the longitude and latitude directions in Figure 4a,c, respectively.

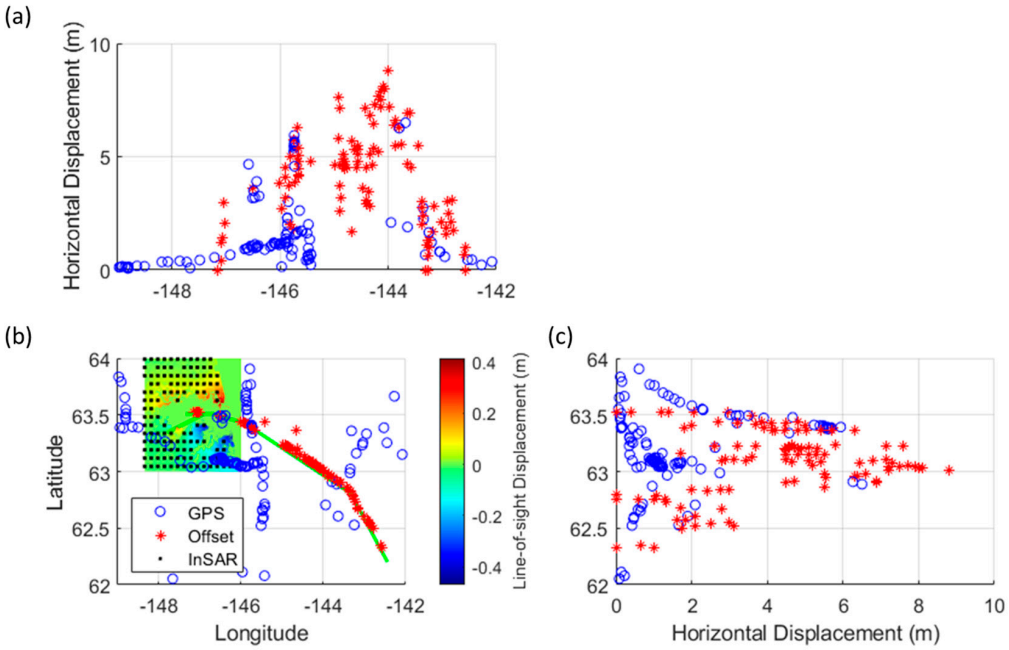

Figure 3. Spatial distribution of dataset and comparison of horizontal GPS and offset measurements: (**a**) horizontal displacements along longitude; (**b**) map view of the GPS, offset, and InSAR data; and (**c**) horizontal displacements along latitude.

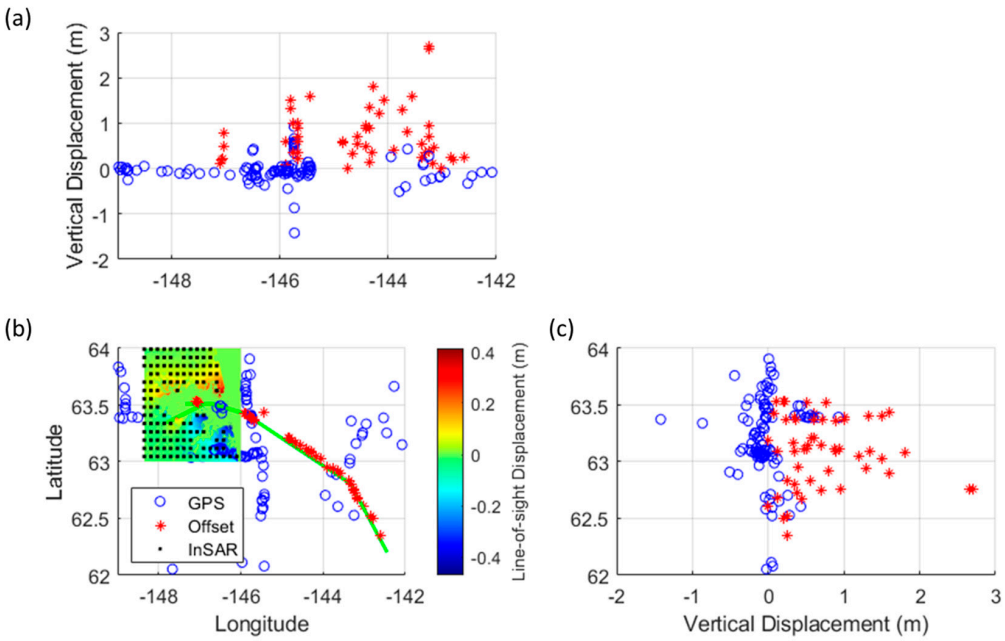

Figure 4. Spatial distribution of dataset and comparison of vertical GPS and offset measurements: (**a**) horizontal displacements along longitude; (**b**) map view of the GPS, offset, and InSAR data; and (**c**) vertical displacements along latitude.

Table 3. Model parameters of the fault planes considered in the benchmark studies. SG indicates the Susitna Glacier fault, and TC indicates the Totschunda fault.

	No. of Segments	Strike (Degree)	Dip (Degree)	Rake (Degree)	Length (km)	Width (km)	Size of Subfaults (km)
Wright et al. [34]	9	SG 1-2: 249.6° Denali 1: 98.3° Denali 2: 105.1° Denali 3: 119° Denali 4: 108.4° Denali 5: 114.9° Denali 6: 116.8° Denali 7: 151.2° TC: 135.3°	SG 1-2: 41° Denali-TC: 90°	SG 1-2: 84.6° Denali-TC: 180°	SG 1-2: 28.5 Denali 1: 47 Denali 2: 20.3 Denali 3: 22.2 Denali 4: 31.6 Denali 5: 39.6 Denali 6: 51.1 Denali 7: 20.8 TC: 49.7	SG 1-2: 10 Denali-TC: 16	Strike direction: SG: 4.06 Denali 1: 3.92 Denali 2: 4.06 Denali 3: 3.7 Denali 4: 3.95 Denali 5: 3.96 Denali 6: 3.96 Denali 7: 4.16 TC: 4.14 Dip direction: SG: 2.5 Denali-TC: 4
Asano et al. [37]	4	SG 1-2: 262° Denali 1: 279° Denali 2: 298° TC: 315°	SG 1-2: 48° Denali-TC: 86°	SG 1-2: 174.8° Denali-TC: 122°	SG 1-2: 31.5 Denali 1: 72 Denali 2: 126 TC: 63	18	Both strike and dip directions: 4.5
Hreinsdóttir et al. [39]	11	SG 1: 262° SG 2: 262° Denali 1: 261° Denali 2: 279° Denali 3: 286° Denali 4: 300° Denali 5: 290° Denali 6: 297° Denali 7: 300° TC 1: 335° TC 2: 320°	SG 1: 19° SG 2: 48° Denali-TC: 89.99°	SG 1-2: 84.6° Denali-TC: 180°	SG 1-2: 33 Denali 1: 32 Denali 1: 40 Denali 1: 146 TC: 83	SG 1: 6.14 SG 2: 8.88 Denali-TC: 18	Both strike and dip directions: 3

A model-weighted error is calculated for each generated source model and benchmark study based on Equation (2), and sources that have better matches with the observations (lower weighted errors) than the benchmark studies are selected. The selected source models are utilized to generate surface displacement maps.

$$\begin{aligned} Weighted\ Error \quad &= w_{InSAR}\sum(InSAR\ Observation - InSAR\ Prediction)^2 \\ &+w_{GPS}\sum(GPS\ Observation - GPS\ Prediction)^2 \\ &+w_{Offset}\sum(Offset\ Observation - Offset\ Prediction)^2. \end{aligned} \tag{2}$$

The InSAR predictions of the generated sources (horizontal and vertical components) are projected to the LOS direction (D_{LOS}) based on Equation (3) and compared with the InSAR observations.

$$D_{LOS} = D_{EW}\cos\alpha\sin\theta + D_{NS}\sin\alpha\sin\theta + D_Z\cos\theta. \tag{3}$$

where D_{EW} is the east–west displacement component, D_{NS} is the north–south displacement component, and D_Z is the vertical displacement component. α is the azimuth angle and θ is the look angle of the satellite. The aforementioned procedure for fault displacement analysis using stochastic source modeling is presented in Figure 5.

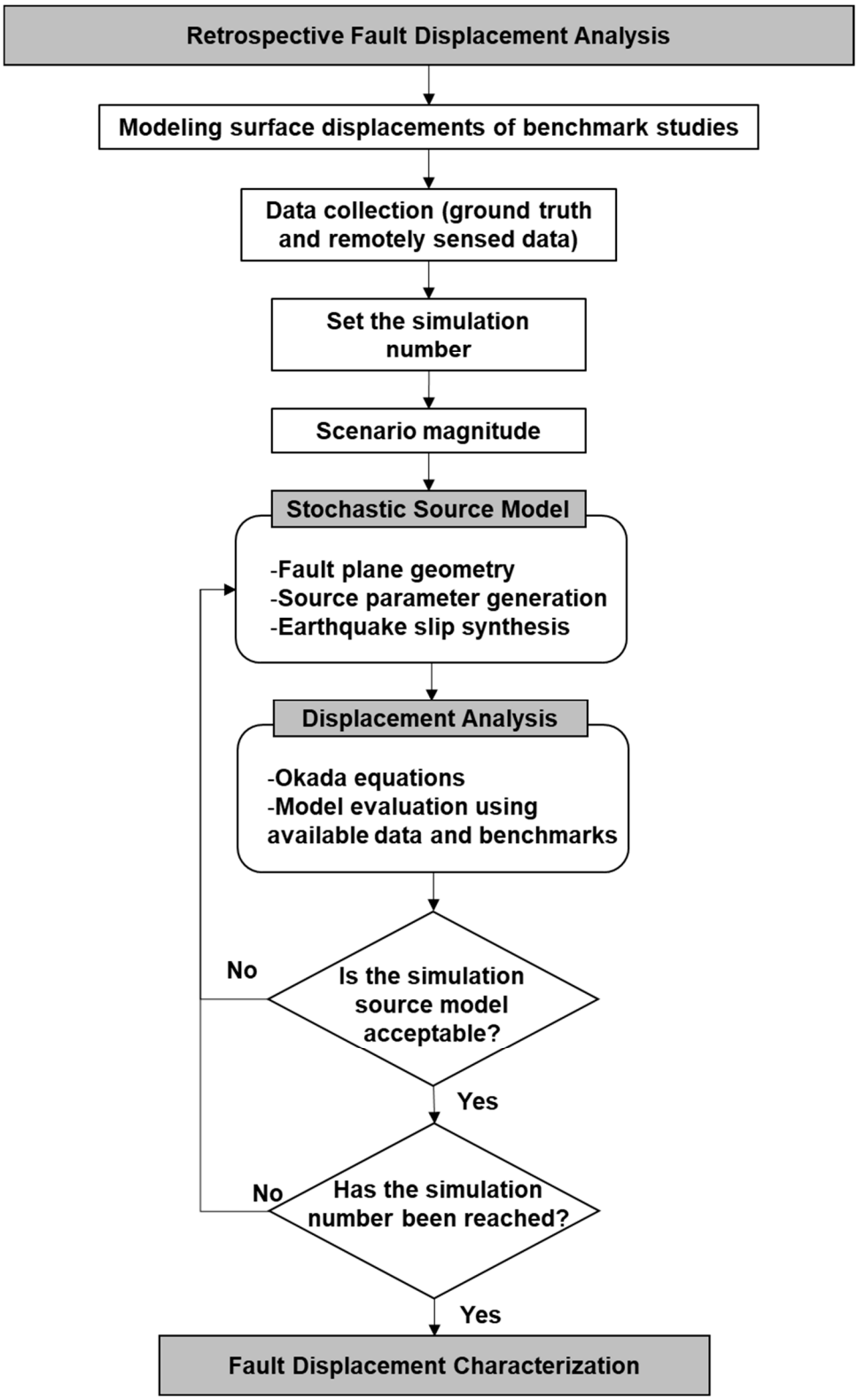

Figure 5. Schematic procedure of the fault displacement characterization of stochastic source modeling.

4. Results

The fault geometry responsible for the 2002 Denali earthquake is modeled with five segments. Table 4 shows the properties of the modeled segments. The modeled geometry is based on the observed surface ruptures (red lines in Figure 1) and the simplest combination

of the geometries introduced by [34,36,37,39]. The assumed fault plane is divided into 1575 subfaults to create a realistic representation, and stochastic source models are generated by utilizing the eight source parameters. The parameters are synthesized based on the statistical scaling relationships (Tables 1 and 2). The magnitude range between 7.8 and 8.0 is considered, and the earthquake magnitudes of each trial are selected randomly within this range. For the selected magnitude range, 20,000 stochastic source models are generated based on the criteria outlined in the following. Figure 6 demonstrates the 20,000 sampled source parameters out of more than 1.9 million source model evaluations for the earthquake magnitude, Mw 7.9 $\pm$ 0.1. The discrete patterns of the fault length, as depicted in Figure 6a, are due to the limitation of the fault dimensions to odd multiples of the subfault size, which is set to 2 km in this study. Therefore, the fault lengths can be 2 km, 6 km, 10 km, etc. This necessity for odd multiples of the subfault size is a requirement originating from the process of generating wavenumber vectors in the earthquake slip synthesis method proposed by [51]. In this method, the wavenumber is specified at lower and upper boundary wavenumbers, as well as at a zero wavenumber.

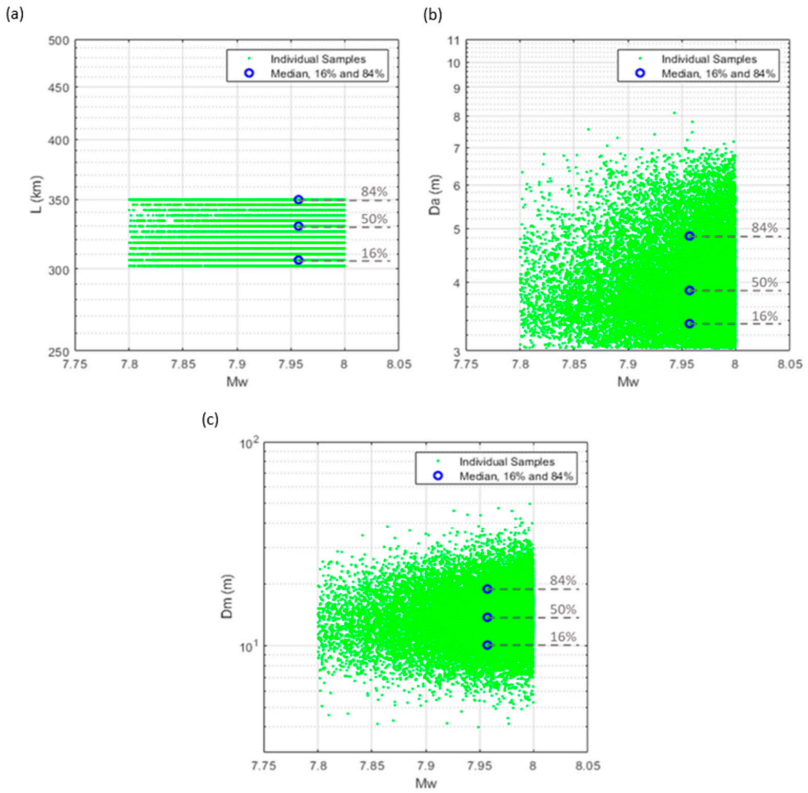

Figure 6. Sampled source parameters of stochastic earthquake models for the (**a**) fault length, (**b**) mean slip, and (**c**) maximum slip.

Table 4. Geometry of the 2002 Denali earthquake fault model.

Segment Number	Segment	Strike (Degree)	Dip (Degree)	Rake (Degree)	Length (km)	Width (km)
1	Susitna Glaciers	248°	48°	135°	48	18
2	Denali-1	270°	85°	175°	32	18
3	Denali-2	284°	85°	175°	40	18
4	Denali-3	299°	85°	175°	147	18
5	Totschunda	326°	85°	175°	81	18

The selection of the 20,000 source models among the 1.9 million simulations is based on various criteria that reflect the seismological knowledge of the target region and previous studies. The constraints are the asperity zone along the strike (limited to the Denali-2 and Denali-3 segments), the required slip in the asperity zone (50% to 100% maximum slip), the ratio of the length to the width of the fault plane (0.5 to 20), the ratio of the high-slip area to the total area of the fault plane (0.148 to 0.332), the length of the fault (300 km to 350 km), and the range of the stochastic source parameters (0.15 to 0.45 for the ratio of the along-dip correlation length to the fault width and 0.15 to 1 for the ratio of the along-strike correlation length to the fault length). More information can be found in [50]. The overall slip characteristics of the generated stochastic source models are illustrated in Figure 7. The figure depicts the average of the 20,000 source models, which are refined based on the mentioned constraints, for the earthquake scenario. The average slip distribution captures the variations in the slip values, the trend of the slip distribution, and the spatial extents of the earthquake slip distributions.

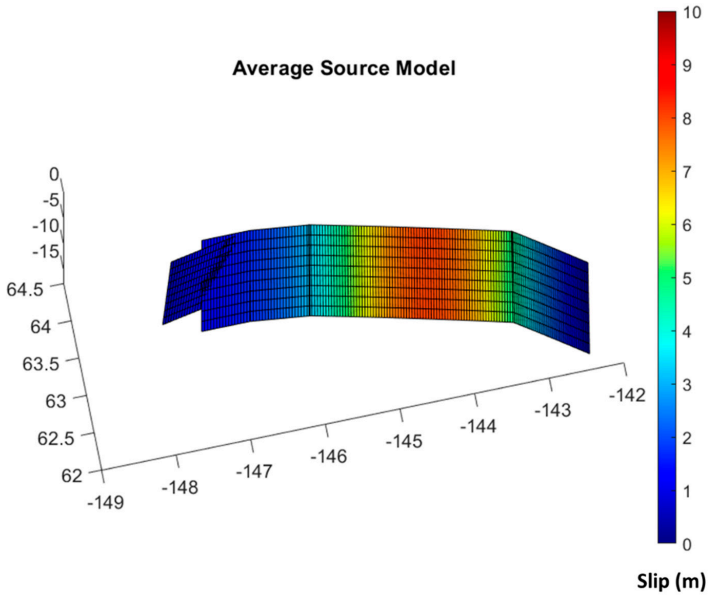

Figure 7. The average model out of 20,000 generated stochastic source models.

To evaluate the performance of the generated source models in characterizing the surface displacement of the 2002 Denali earthquake, the weighted errors of the generated sources are compared with the weighted errors of the three benchmark studies [34,37,39]. In order to investigate the effect of each dataset in the earthquake source characterization, we first generate the best source models from the offset, GPS, and InSAR data individually and compare the properties of the resulting source models. Then, we simulate the source models using all three datasets and compare the results with the case of the individual dataset. The calculated weighted errors, together with those of the three benchmark studies, are listed in Table 5. It should be mentioned that the benchmark studies only provide the source models, and we have calculated the surface displacements using the Okada equations for the comparisons. The weighted errors of the 20,000 generated source models are calculated based on Equation (2). The weights associated with each dataset are considered as 1 in the present study.

Source models with total weighted errors (the sum of the weighted errors in all categories) lower than the total of the baseline (the sum of the minimum weighted errors of the benchmark studies for individual observation categories) are selected. The number of selected sources is 17. Table 5 shows the model-weighted errors of the three studies, along with the generated source models for the cases of individual and integrated datasets (SSM-3748 for the offset data, SSM-4813 for the GPS data, SSM-1432 for the InSAR data, and

SSM-3979 for the integrated data). Once the performance of the stochastic source modeling method is validated by the benchmark studies, the effect of the considered datasets on the source simulations is studied.

Figure 8b–d, Figure 9b–d, Figures 10b–d and 11b–d are illustrations of the three orthogonal components of the surface displacements calculated with the Okada equations for the proposed source models of SSM-3748, SSM-4813, SSM-1432, and SSM-3979, respectively. Similar to the benchmark studies, the right-lateral motion is visible in the case of all source models. Figure 8e,f, Figure 9e,f, Figure 10e,f and Figure 11e,f show the comparison of the surface displacements of the modeled sources with the GPS data for the horizontal and vertical components, respectively. Figure 8g,h, Figure 9g,h, Figure 10g,h and Figure 11g,h display the comparison of the modeled offset data with the field geological measurements. Simulated stochastic models are capable of quantifying the range of possibilities in GPS stations as well as near-field regions.

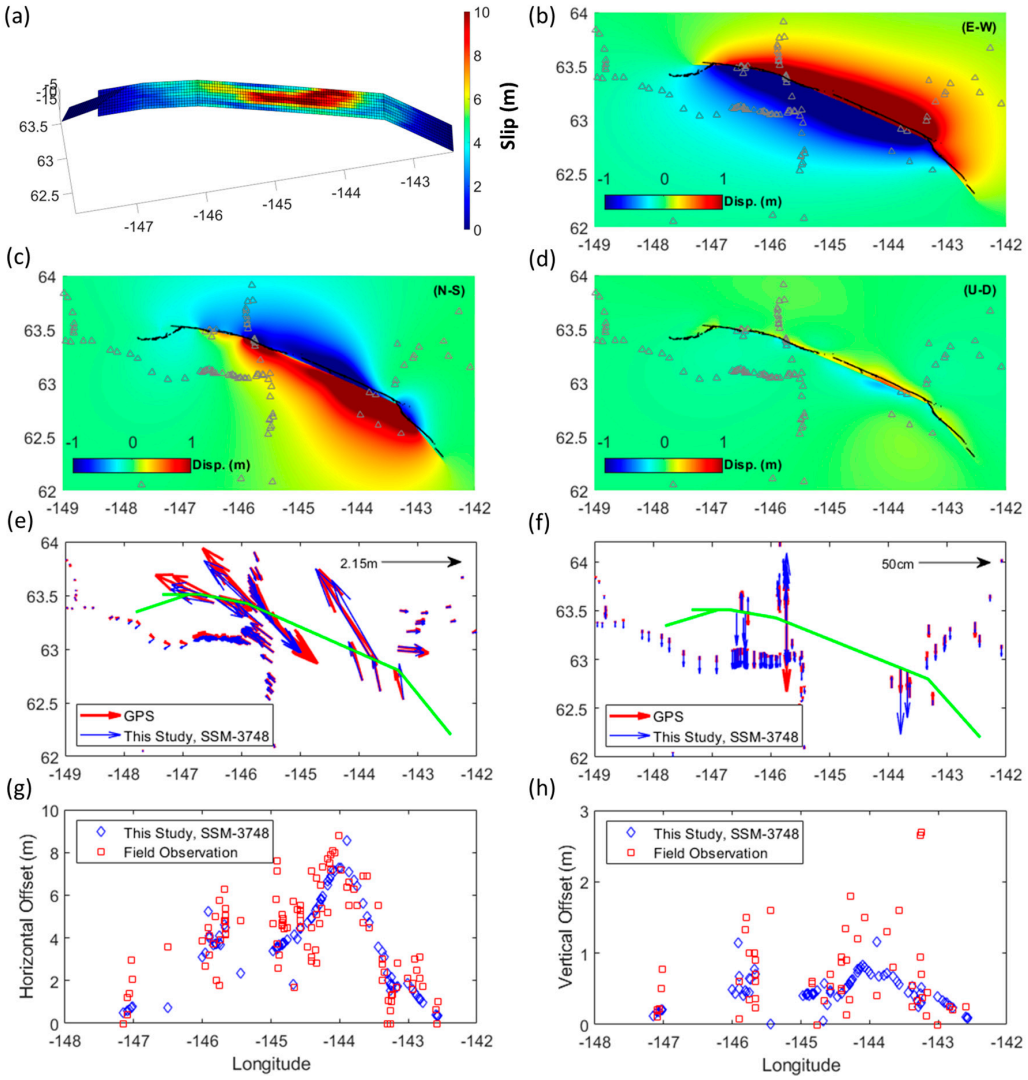

Figure 8. Simulated surface displacements of the 2002 Denali earthquake for SSM-3748 for (**a**) earthquake slip distribution, (**b**) Okada surface displacement in east–west (E-W) direction, (**c**) Okada surface displacement in north–south (N-S) direction, (**d**) Okada surface displacement in up–down (U-D) direction (the black lines indicate mapped surface ruptures [44], and the grey triangles show the GPS stations used in the present study), (**e**) horizontal GPS displacement vectors, (**f**) vertical GPS displacement vectors (the green lines show the modeled fault trace), (**g**) horizontal offsets along the fault trace, and (**h**) vertical offsets along the fault trace.

Table 5. Model-weighted errors of the benchmark studies and stochastic source models.

Model-Weighted Error	Wright et al. [34]	Asano et al. [37]	Hreinsdóttir et al. [39]	Baseline of Benchmark Studies	SSM-3748 (Offset)	SSM-4813 (GPS)	SSM-1432 (InSAR)	SSM-3979 (Integrated)
Offset H	213.36	77.58	61.6	61.6	47.72	55.24	104.68	55.01
Offset Z	11.73	7.78	25.87	7.78	6.40	7.80	7.94	6.78
GPS H	19.28	72.50	3.43	3.43	5.81	2.58	39.31	3.00
GPS Z	2.66	2.23	1.71	1.71	1.15	1.04	1.55	1.13
InSAR	2.28	4.4	4.99	2.06	1.27	1.87	0.52	1.53
Total	249.31	164.49	97.60	76.58	62.35	68.53	154.00	67.45

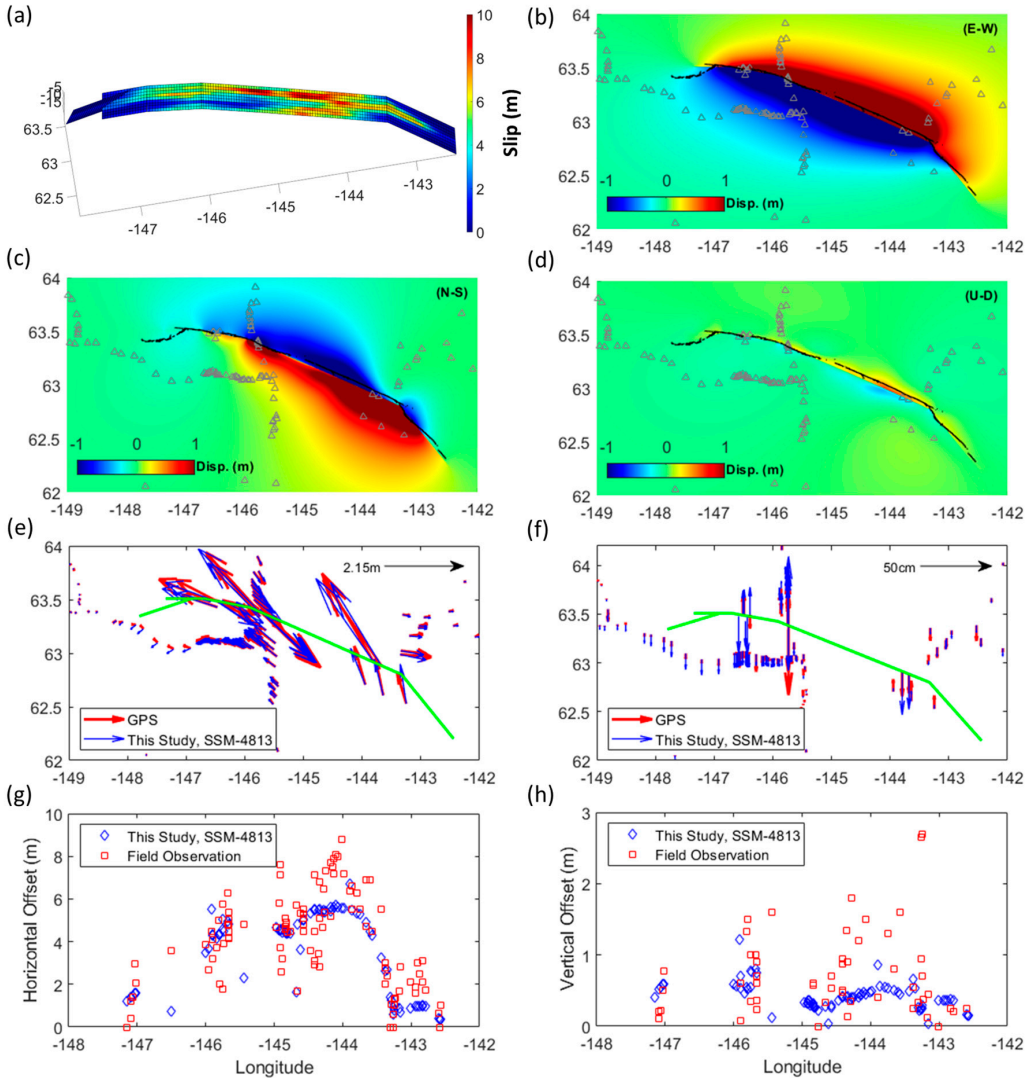

Figure 9. Simulated surface displacements of the 2002 Denali earthquake for SSM-4813 for (**a**) earthquake slip distribution, (**b**) Okada surface displacement in east–west (E-W) direction, (**c**) Okada surface displacement in north–south (N-S) direction, (**d**) Okada surface displacement in up–down (U-D) direction (the black lines indicate mapped surface ruptures [44], and the grey triangles show the GPS stations used in the present study), (**e**) horizontal GPS displacement vectors, (**f**) vertical GPS displacement vectors (the green lines show the modeled fault trace), (**g**) horizontal offsets along the fault trace, and (**h**) vertical offsets along the fault trace.

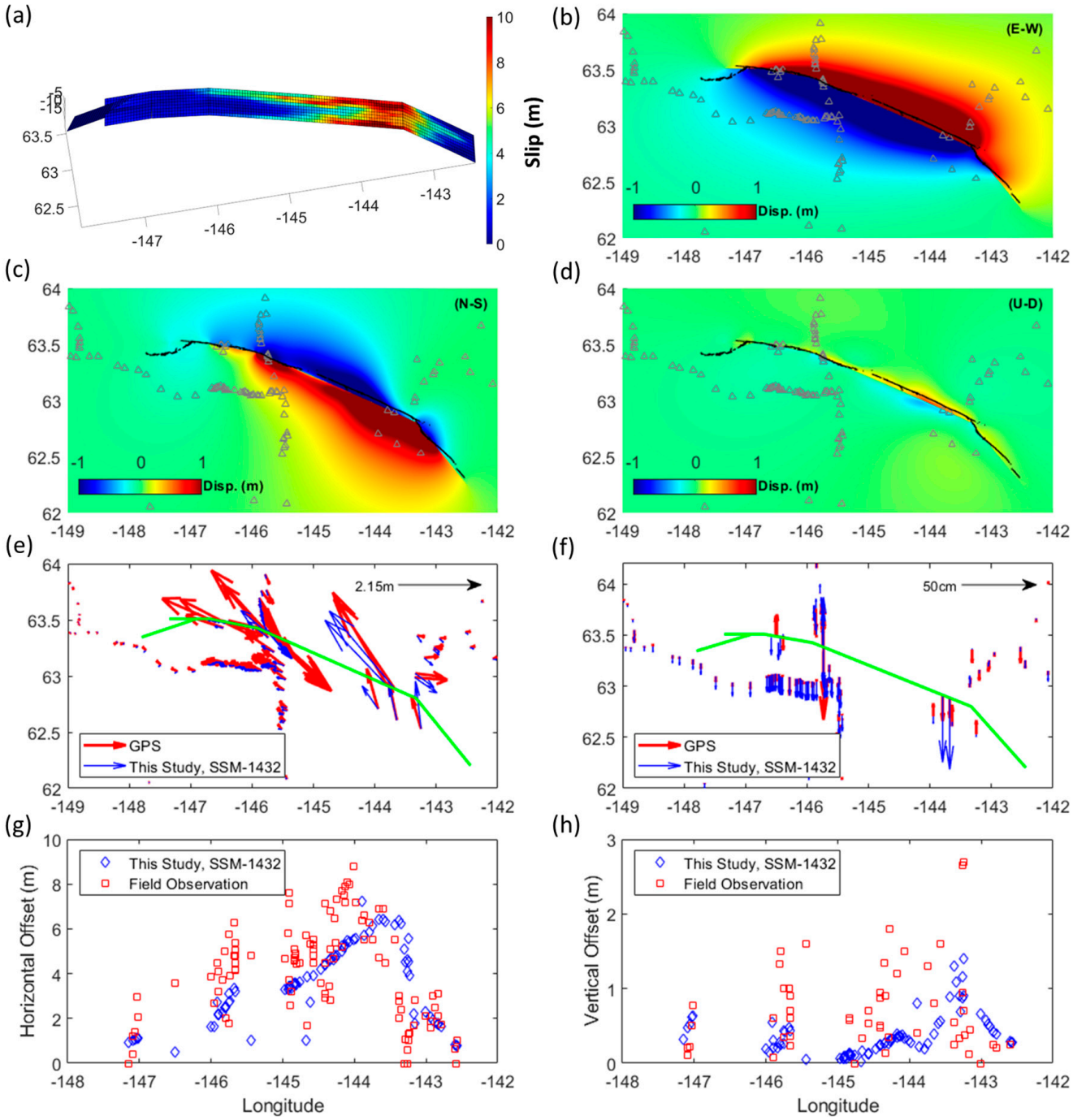

Figure 10. Simulated surface displacements of the 2002 Denali earthquake for SSM-1432 for (**a**) earthquake slip distribution, (**b**) Okada surface displacement in east–west (E-W) direction, (**c**) Okada surface displacement in north–south (N-S) direction, (**d**) Okada surface displacement in up–down (U-D) direction (the black lines indicate mapped surface ruptures [44], and the grey triangles show the GPS stations used in the present study), (**e**) horizontal GPS displacement vectors, (**f**) vertical GPS displacement vectors (the green lines show the modeled fault trace), (**g**) horizontal offsets along the fault trace, and (**h**) vertical offsets along the fault trace.

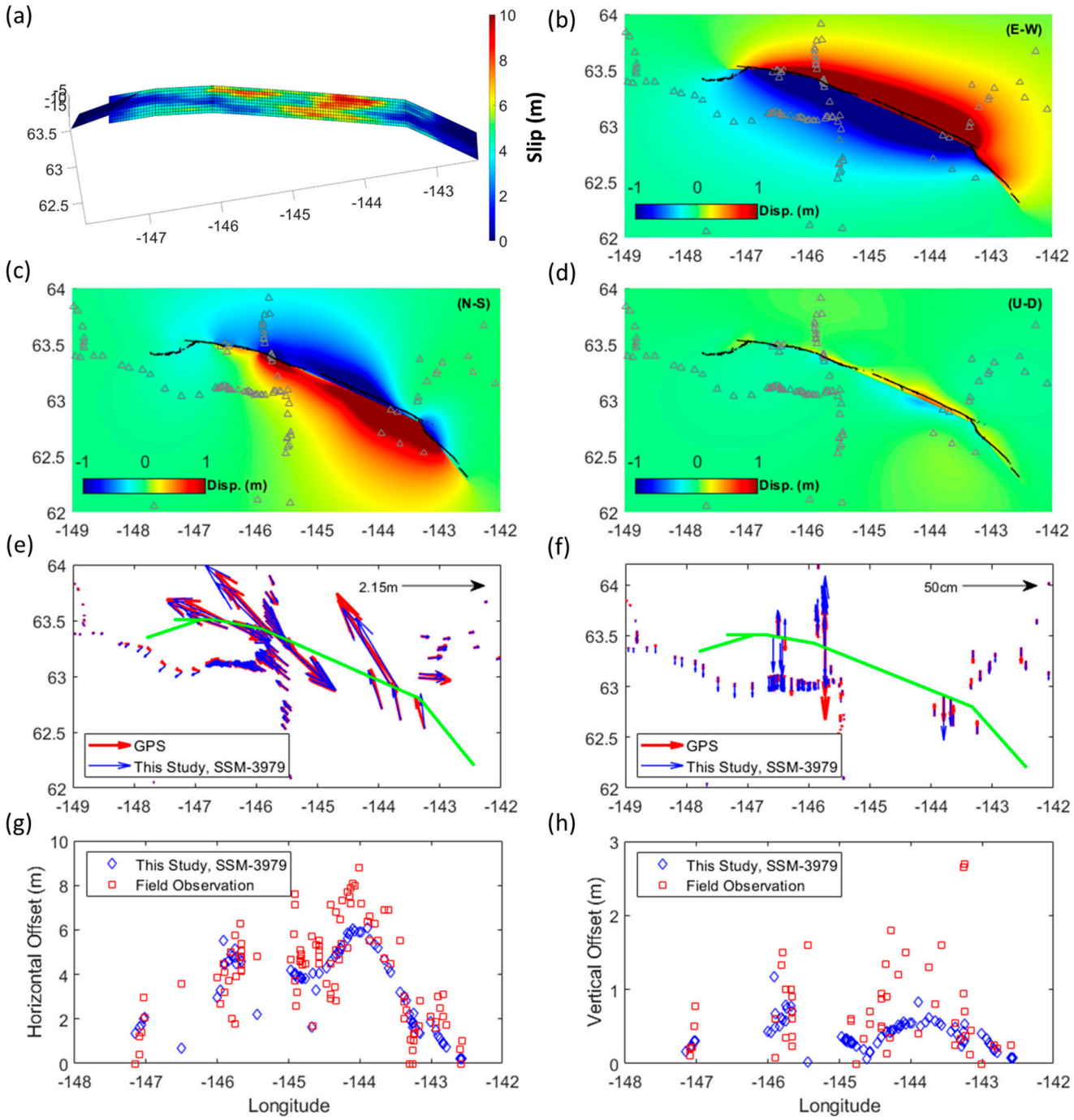

Figure 11. Simulated surface displacements of the 2002 Denali earthquake for SSM-3979 (**a**) earthquake slip distribution, (**b**) Okada surface displacement in east–west (E-W) direction, (**c**) Okada surface displacement in north–south (N-S) direction, (**d**) Okada surface displacement in up–down (U-D) direction (the black lines indicate mapped surface ruptures [44], and the grey triangles show the GPS stations used in the present study), (**e**) horizontal GPS displacement vectors, (**f**) vertical GPS displacement vectors (the green lines show the modeled fault trace), (**g**) horizontal offsets along the fault trace, and (**h**) vertical offsets along the fault trace.

5. Discussion

Based on Figure 8g,h, Figure 9g,h, Figure 10g,h and Figure 11g,h, the slip distribution of SSM-3748 (Figure 8a) shows higher values than the slip distributions of SSM-4813 (Figure 9a), SSM-1432 (Figure 10a), and SSM-3979 (Figure 11a). This is because the offset

data are higher in value than the GPS and InSAR data; hence, the source model generated using these data represents higher slip values. Moreover, the slip distribution of SSM-4813 shows higher spatial variation along the fault plane (Figure 9a). The reason is that the GPS data are more scattered in the rupture areas; therefore, the corresponding source model shows higher spatial variation. The slip distribution of SSM-1432 (Figure 10a) is not reliable due to the lack of InSAR data in the eastern part of the fault. This source can contribute to the slip characterization of the western part of the fault. The location of the asperity zone in the eastern part can be due to the lower displacement of the InSAR data in the western end of the rupture. The slip distribution of the integrated data (Figure 11a) captures all the features of the slip distribution associated with the individual datasets. Comparing the modeled displacements at the GPS stations with the field offset measurement points (Figure 8e–h, Figure 9e–h, Figure 10e–h, Figure 11e–h), it can be noted that SSM-3748 has a better match with the offset data, SSM-4813 has a better match with the GPS data, and SSM-1432 has a better match with the InSAR data.

In general, the generated source models demonstrate that there is large along-strike variation in the slip values. Furthermore, the slip values vary more in the shallow and deep patches in comparison to the center of the fault plane. The generated source models demonstrate that there is large along-strike variation in the slip values in the Denali fault. The slip in the Susitna Glaciers fault is generally lower than 2 m. The first two segments of the Denali fault have ~6 m slips in general. There are two main asperity zones in the central strike-slip segment, between 120 km and 270 km along the fault trace. This feature is visible in the source models associated with [34,39]. The maximum slip of the primary asperity zone is about 10 m at the depth of 10 to 18 km and a slip of 6 m near the surface. The second is close to the junction of the Denali and Totschunda faults and has a higher slip at a shallower depth and ~9 m slip near the surface.

The results of this study demonstrate the impact of integrating datasets in stochastic source modeling and subsequent fault displacement assessment using the case study of the 2002 Denali earthquake. Based on Table 5, the integrated case (SSM-3979) has lower model-weighted errors than the baseline in each category, and SSM-3748 has the lowest total weighted errors. It is also inferred from Table 5 that the average differences in SSM-3748, SSM-4813, SSM-1432, and SSM-3979 from the baseline are –8.40%, –16.65%, 206.79%, and –19.15%, respectively. The average differences are calculated by deriving the relative differences from the baseline for each category of the dataset and multiplying this by the weight values of each category and then taking the average weighted errors for each source model. The source models using GPS and integrated data have a noticeable decrease in the model-weighted errors from the baseline.

It is also inferred from the table that SSM-3748 has a lower total weighted error than the integrated datasets. The reason is that the model-weighted error, which is the residual sum of squares, depends on the values of the parameters in the model. Since offset data have larger displacement values, the model-weighted error is higher than in other categories with smaller values. Therefore, in the case of the source model considering offset data, there is a significant decrease in the offset categories (Offset H and Offset Z), which leads to a smaller total weighted error.

One of the main problems in the procedure of simulating stochastic source models was the match of the generated surface displacements with the GPS H and Offset Z data. The sources with a good match with the GPS H data showed the opposite behavior regarding the Offset Z data. Figure 12 shows the model-weighted errors for the two Offset Z and GPS H. The mentioned effect is more noticeable in the benchmark studies. The study of Hreinsdóttir et al. [39] provides the minimum model-weighted error among the benchmark studies in the GPS H category. At the same time, it has the highest model-weighted error in the Offset Z category.

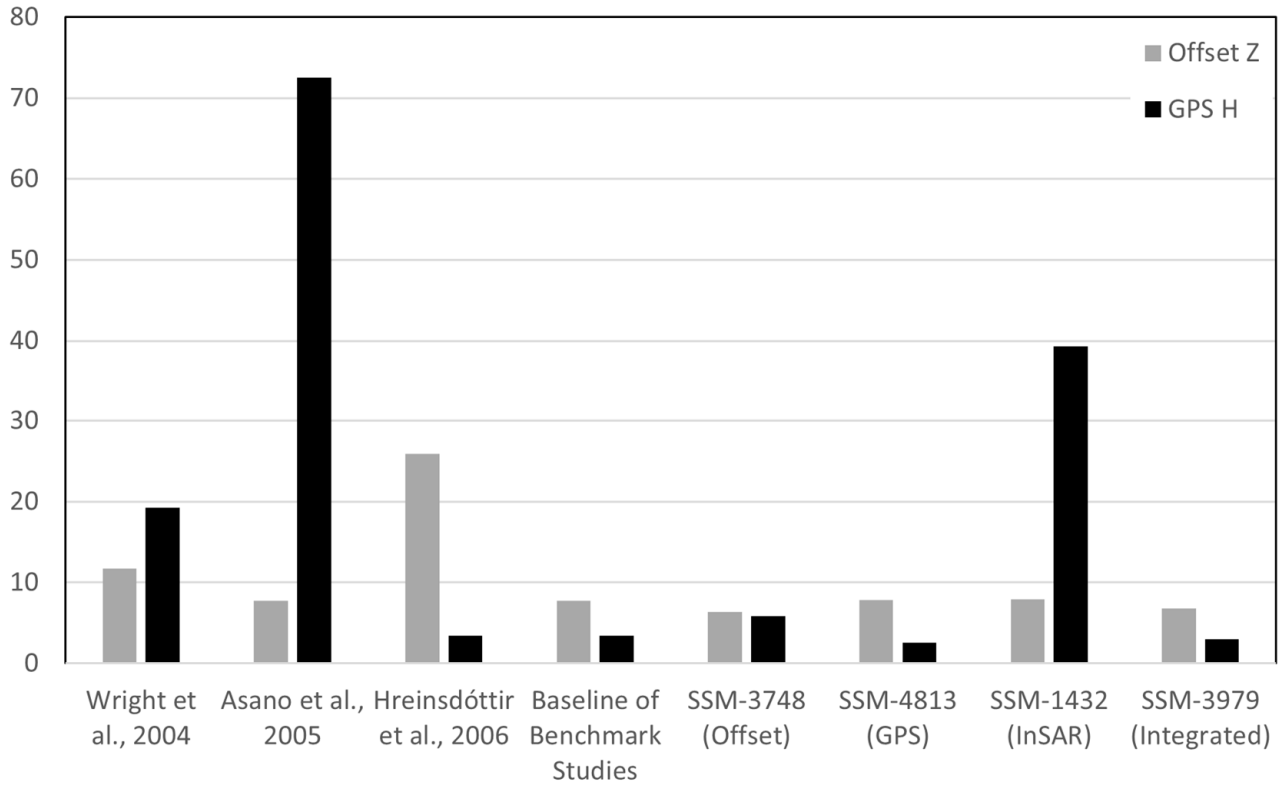

Figure 12. Distribution of model-weighted errors of Offset Z and GPS H among benchmark studies ([34,37,39]) and simulated stochastic sources.

This feature can be explained by comparing the two datasets shown in Figures 3 and 4. Based on Figure 3, the maximum values of GPS H are around 146° W longitude and between 63° N and 63.5° N latitude. In contrast, based on Figure 4, the maximum values of Offset Z are between 145° W and 143° W longitude and between 62.5° N and 63° N latitude. This discrepancy affects the locations of the asperity zones along the fault plane in the fault models. The probable reason for this inconsistency is the lack of GPS data between 145.5° W and 144° W longitude in the vicinity of the fault trace, where the maximum surface ruptures are recorded.

Figure 13a–d display histograms of the weighted errors of the simulated stochastic source models for the offset, GPS, and InSAR data, along with the total weighted error considering all datasets, respectively. Vertical lines represent the model-weighted errors of the selected sources and the baseline (see Table 5). The probability of higher weighted errors is greater for field observations, whereas the GPS and InSAR data are more likely to yield lower weighted errors. This discrepancy may arise mainly from the fact that field observations involve larger displacement values along the fault trace, and the uncertainty associated with field observations is higher than that for GPS data. Consequently, it is expected that the selected results align more closely with the GPS data than with the field observations. This is also inferred from the lower number of generated sources with model-weighted errors smaller than the baseline of the GPS data (Figure 13b). This means that GPS data further constrain the source selection. Nevertheless, the total weighted errors are mainly influenced by the field observations. The source selection procedure is based not only on the total model-weighted error being lower than the baseline, but also on the model-weighted errors being lower than the baseline in each individual category. The lowest model-weighted error belongs to the source model that is generated using the same dataset of each histogram.

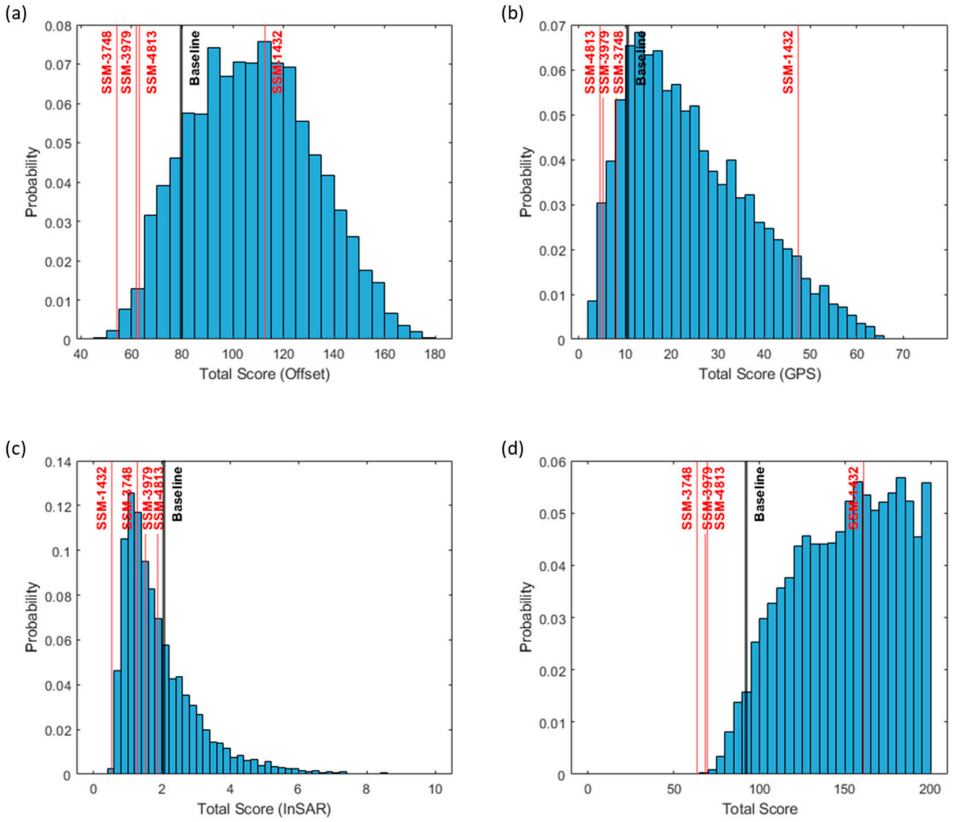

Figure 13. Histogram of weighted errors of the stochastic source models for (**a**) field observations, (**b**) GPS, (**c**) InSAR, and (**d**) all datasets. Weighted errors of SSM-3748, SSM-4813, SSM-1432, and SSM-3979 are shown with red lines, and weighted errors of baseline are shown with black lines.

6. Conclusions

This study investigated the impact of ground truth and remotely sensed data and their interplay regarding the performance of the stochastic source modeling method in the generation of realistic earthquake surface deformation. The method was applied to the Mw 7.9 Denali earthquake in Alaska, United States, on 3 November 2002. Stochastic source models were generated and the corresponding surface displacements were obtained using the Okada equations. Then, source models were selected based on the best match of the associated surface displacements with the available datasets. The performance of the method in generating surface displacements was compared with that demonstrated in benchmark studies.

The results of the case study of the 2002 Denali earthquake indicate that the combined use of the available datasets can contribute to improving the performance of the method in generating stochastic source models. Furthermore, GPS data can leverage the performance of the method more than offset and InSAR data. Based on the obtained results, the average differences in the model-weighted errors for source models using offset, GPS, and InSAR data from the baseline are -8.40%, -16.65%, and 206.79%, respectively, and that for the case of the integrated source model is -19.15%, which is close to the performance of the source model using the GPS data. Therefore, in the case of using a single dataset, GPS data can provide a reasonable approximation of the earthquake solution. The sufficiency of a specific dataset is dependent on factors such as the uncertainty, the spatial coverage of the data, and the time frame of the measurements, which can vary for other earthquakes.

As elaborated in the Results section, source SSM-3748 (generated using offset data) indicates the concentration of slip in the vicinity of the observed maximum surface rupture, while SSM-3748 (generated using GPS data) represents the variability in slip in the asperity zone, and source SSM-1432 is not reliable due to the lack of InSAR data in the eastern part

of the rupture, where the asperity zone of the earthquake is located. Source SSM-3979 (generated using integrated data) depicts all the features of the slip distribution associated with the individual datasets.

Although the results are obtained from a case study of the 2002 Denali earthquake, the inclusion of different datasets may not always improve the performance of the method in other scenarios. The uncertainties of the dataset can be accumulated and reduce the efficiency of the method. However, there is cross-validation in the source selection procedure, which reduces the effect of these uncertainties. The impact of uncertainties will be further investigated in future studies. Furthermore, the stochastic source modeling approach can be enhanced for the connecting areas of faults with different mechanisms (the connecting area of the Susitna Glaciers fault and the Denali fault, which is an example of an inter-connected fault system). Moreover, the methodology can be developed to include segmentation and different seismic moment releases of individual segments. The authors' future studies will focus on developing the proposed method for the case of complex fault systems. The improved performance of the stochastic source modeling in surface fault displacement characterization can contribute to designing critical infrastructure crossing the fault trace and assessing its structural integrity against possible differential fault displacement hazards.

Author Contributions: P.S. and K.G. contributed to the conceptualization and design of the research plan. Analyses and original draft preparation were performed by P.S. Supervision, reviewing, and editing of the previous versions of the manuscript were conducted by K.G. All authors have read and agreed to the published version of the manuscript.

Funding: This study is supported by the Canada Research Chair program (CRC-2022-00081) and the NSERC Discovery Grant (RGPIN-2024-04428).

Data Availability Statement: The interferometric data of the 2002 Denali earthquake were provided by Tim Wright. The USGS 30 m DEM was used for the mapping of the study area (https://portal.opentopography.org, last access 8 October 2023). All other information is included in the main text.

Acknowledgments: The authors are grateful to the authoritative reviewers, whose comments significantly improved the quality of this study.

Conflicts of Interest: The authors declare no competing interests.

Appendix A

For a finite rectangular fault (Figure A1), the surface displacements can be derived from Equations (A1) to (A6), which are based on the study of Okada [49].

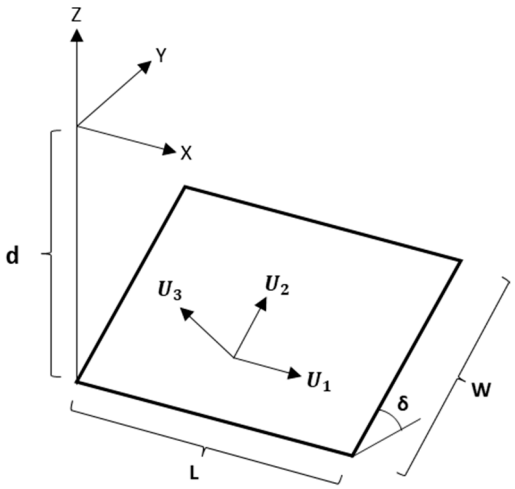

Figure A1. Geometry of the fault.

For a strike-slip fault,

$$\begin{cases} u_x = -\frac{U_1}{2\pi}\left[\frac{\xi q}{R(R+\eta)} + \tan^{-1}\frac{\xi\eta}{qR} + I_1 \sin\delta\right] \\ u_y = -\frac{U_1}{2\pi}\left[\frac{\widetilde{y} q}{R(R+\eta)} + \frac{q\cos\delta}{R+\eta} + I_2 \sin\delta\right] \\ u_z = -\frac{U_1}{2\pi}\left[\frac{\widetilde{d} q}{R(R+\eta)} + \frac{q\sin\delta}{R+\eta} + I_4 \sin\delta\right]. \end{cases} \tag{A1}$$

For a dip-slip fault,

$$\begin{cases} u_x = -\frac{U_2}{2\pi}\left[\frac{q}{R} - I_3 \sin\delta\cos\delta\right] \\ u_y = -\frac{U_2}{2\pi}\left[\frac{\widetilde{y} q}{R(R+\xi)} + \cos\delta\tan^{-1}\frac{\xi\eta}{qR} - I_1 \sin\delta\cos\delta\right] \\ u_z = -\frac{U_2}{2\pi}\left[\frac{\widetilde{d} q}{R(R+\xi)} + \sin\delta\tan^{-1}\frac{\xi\eta}{qR} + I_5 \sin\delta\cos\delta\right]. \end{cases} \tag{A2}$$

For a tensile fault,

$$\begin{cases} u_x = \frac{U_3}{2\pi}\left[\frac{q^2}{R(R+\eta)} - I_3(\sin\delta)^2\right] \\ u_y = \frac{U_3}{2\pi}\left[\frac{\widetilde{d} q}{R(R+\xi)} + \sin\delta\left\{\frac{\xi q}{R(R+\eta)} - \tan^{-1}\frac{\xi\eta}{qR}\right\} + I_1(\sin\delta)^2\right] \\ u_z = \frac{U_3}{2\pi}\left[\frac{\widetilde{y} q}{R(R+\xi)} + \cos\delta\left\{\frac{\xi q}{R(R+\eta)} - \tan^{-1}\frac{\xi\eta}{qR}\right\} + I_5(\sin\delta)^2\right]. \end{cases} \tag{A3}$$

where

$$\begin{cases} \begin{pmatrix} I_1 = \binom{\mu}{\lambda+\mu}\left[\binom{-1}{\cos\delta}\binom{\xi}{R+\widetilde{d}}\right] - \binom{\sin\delta}{\cos\delta} I_5 \\ I_2 = \binom{\mu}{\lambda+\mu}[-\ln(R+\eta)] - I_3 \end{pmatrix} \\ I_3 = \frac{\mu}{\lambda+\mu}\left[\frac{1}{\cos\delta}\frac{\widetilde{y}}{R+\widetilde{d}} - \ln(R+\eta)\right] + \frac{\sin\delta}{\cos\delta} I_4 \\ \begin{pmatrix} I_4 = \binom{\mu}{\lambda+\mu}\binom{1}{\cos\delta}\left[\ln\left(R+\widetilde{d}\right) - \sin\delta ln(R+\eta)\right] \\ I_5 = \binom{\mu}{\lambda+\mu}\binom{2}{\cos\delta}\tan^{-1}\binom{\eta(X+q\cos\delta)+X(R+X)\sin\delta}{\xi(R+X)\cos\delta} \end{pmatrix} \end{cases} \tag{A4}$$

and, if $\cos\delta = 0$,

$$\begin{cases} \begin{pmatrix} I_1 = -\binom{\mu}{2(\lambda+\mu)}\binom{\xi q}{\left(R+\widetilde{d}\right)^2} \\ I_3 = -\binom{\mu}{2(\lambda+\mu)}\left[\binom{\eta}{R+\widetilde{d}} + \binom{\widetilde{y} q}{\left(R+\widetilde{d}\right)^2} - \ln(R+\eta)\right] \end{pmatrix} \\ I_4 = -\frac{\mu}{\lambda+\mu}\frac{q}{R+\widetilde{d}} \\ I_5 = -\frac{\mu}{\lambda+\mu}\frac{\xi\sin\delta}{R+\widetilde{d}} \end{cases} \tag{A5}$$

$$\begin{cases} p = y\cos\delta + d\sin\delta \\ q = y\sin\delta - d\cos\delta \\ \widetilde{y} = \eta\cos\delta + q\sin\delta \\ \widetilde{d} = \eta\sin\delta - q\cos\delta \\ R^2 = \xi^2 + \eta^2 + q^2 = \xi^2 + \widetilde{y}^2 + \widetilde{d}^2 \\ X^2 = \xi^2 + q^2. \end{cases} \tag{A6}$$

where the displacement field u(x,y,z) is due to a dislocation ξ along the length (L) and dislocation η along the width (W). δ is the dip angle; λ and μ are Lame's constants, replaced

by Poisson's ratio ν with a value of 0.25 for an isotropic medium [53]. U_1 , U_2 , and U_3 correspond to strike-slip, dip-slip, and tensile dislocations, and the movement directions shown in Figure A1 are associated with the hanging wall block.

References

1. Yang, S.; Mavroeidis, G.P. Bridges crossing fault rupture zones: A review. *Soil Dyn. Earthq. Eng.* **2018**, *113*, 545–571. [CrossRef]
2. Zheng, Q.; Liu, X.; Zhang, H.; Gu, X.; Fang, M.; Wang, L.; Adeeb, S. Reliability evaluation method for pipes buried in fault areas based on the probabilistic fault displacement hazard analysis. *J. Nat. Gas Sci. Eng.* **2021**, *85*, 103698. [CrossRef]
3. Garcia, F.E. Discrete element analysis of earthquake surface fault rupture through layered media. *Soil Dyn. Earthq. Eng.* **2022**, *152*, 107021. [CrossRef]
4. Melissianos, V.E.; Danciu, L.; Vamvatsikos, D.; Basili, R. Fault displacement hazard estimation at lifeline–fault crossings: A simplified approach for engineering applications. *Bull. Earthq. Eng.* **2023**, *21*, 4821–4849. [CrossRef]
5. Shantz, T.; Alameddine, F.; Simek, J.; Yashinsky, M.; Merriam, M.; Keever, M. Evaluation of fault rupture hazard mitigation. In Proceedings of the 7th National Seismic Conference on Bridges and Highways, Oakland, CA, USA, 20–22 May 2013.
6. Stepp, J.C. Probabilistic seismic hazard analyses for fault displacement and ground motions at Yucca Mountain, Nevada. *Earthq. Spectra* **2001**, *17*, 113–151. [CrossRef]
7. Braun, J.B. Probabilistic Fault Displacement Hazards of the Wasatch Fault. Master's Thesis, University of Utah, Salt Lake City, UT, USA, 2000.
8. Youngs, R.R.; Arabasz, W.J.; Anderson, R.E.; Ramelli, A.R.; Ake, J.P.; Slemmons, D.B.; McCalpin, J.P.; Doser, D.I.; Fridrich, C.J.; Swan, F.H., III; et al. A Methodology for Probabilistic Fault Displacement Hazard Analysis (PFDHA). *Earthq. Spectra* **2003**, *19*, 191–219. [CrossRef]
9. Moss, R.; Ross, Z. Probabilistic Fault Displacement Hazard Analysis for Reverse Faults. *Bull. Seismol. Soc. Am.* **2011**, *101*, 1542–1553. [CrossRef]
10. Takao, M.; Tsuchiyama, J.; Annaka, T.; Kurita, T. Application of Probabilistic Fault Displacement Hazard Analysis in Japan. *J. Jpn. Assoc. Earthq. Eng.* **2013**, *13*, 17–36. [CrossRef]
11. Thompson, S. Fault Displacement Hazard Characterization for OpenSRA, California Energy Commission. 2021. Available online: https://peer.berkeley.edu/sites/default/files/cec_fault_displacement_hazard_report_final-draft_2021-02-26_web.pdf (accessed on 24 September 2024).
12. Katona, T.J. Improved Simplified Engineering Fault Displacement Hazard Evaluation Method for On-Fault Sites. *Appl. Sci.* **2024**, *14*, 8399. [CrossRef]
13. Jonathan, B.; Norman, A.; Jennie, W.L.; Largent, M. Performance-Based Earthquake Engineering Assessment Tool for Gas Storage and Pipeline Systems, California Energy Commission, Publication Number: CEC-500-2024-038. 2020. Available online: https://www.energy.ca.gov/sites/default/files/2024-05/CEC-500-2024-038.pdf (accessed on 24 September 2024).
14. Triantafyllaki, A.; Loukidis, D.; Papanastasiou, P. Design of offshore gas pipelines against active tectonic fault movement. *Soil. Dyn. Earthq. Eng.* **2023**, *166*, 107702. [CrossRef]
15. Wesnousky, S.G. Displacement and geometrical characteristics of earthquake surface ruptures: Issues and implications for seismic hazard analysis and the earthquake rupture process. *Bull. Seismol. Soc. Am.* **2008**, *98*, 1609–1632. [CrossRef]
16. Petersen, M.D.; Dawson, T.E.; Chen, R.; Cao, T.; Wills, C.J.; Schwartz, D.P.; Frankel, A.D. Fault Displacement Hazard for Strike-Slip Faults. *Bull. Seismol. Soc. Am.* **2011**, *101*, 805–825. [CrossRef]
17. Nurminen, F.B. Probability of Occurrence and Displacement Regression of Distributed Surface Rupturing for Reverse Earthquakes. *Front. Earth Sci.* **2020**, *8*, 581605. [CrossRef]
18. Wells, D.L.; Coppersmithn, K.J. New empirical relationships among magnitude, rupture length, rupture width, rupture area, and surface displacement. *Bull. Seismol. Soc. Am.* **1994**, *84*, 974–1002. [CrossRef]
19. Michetti, M.A.; Audemard, M.F.; Marco, S. Future trends in paleoseismology: Integrated study of the seismic landscape as a vital tool in seismic hazard analyses. *Tectonophysics* **2005**, *408*, 3–21. [CrossRef]
20. Hanks, T.C.; Bakun, W.H. A Bilinear Source-Scaling Model for M–log A Observations. *Bull. Seismol. Soc. Am.* **2002**, *92*, 1841–1846. [CrossRef]
21. Shaw, B.E. Constant stress drop from small to great earthquakes in magnitude-area scaling. *Bull. Seismol. Soc. Am.* **2009**, *98*, 871–875. [CrossRef]
22. Zielke, O.; Arrowsmith, R.; Ludwig, L.G.; Akciz, S.O. Slip in the 1857 and Earlier Large Earthquakes Along the Carrizo Plain, San Andreas Fault. *Science* **2010**, *327*, 1119–1122. [CrossRef]
23. Gold, R.D.; Cowgill, E. Deriving fault-slip histories to test for secular variation. *Earth Planet.* **2011**, *301*, 52–64. [CrossRef]
24. Allen, T.; Hayes, G. Alternative Rupture-Scaling Relationships for Subduction Interface and Other Offshore Environments. *Bull. Seismol. Soc. Am.* **2017**, *107*, 1240–1253. [CrossRef]
25. Darragh, R.; Bolt, B. Characterization of Source Parameters and Some Empirical Relations between Them for Kachchh Region, Gujarat, India: Implication of January 26, 2001 Bhuj Earthquake and Its Aftershock Sequence. *Bull. Seismol. Soc. Am.* **1987**, *77*, 1479–1484.
26. Henry, C.; Das, S. Aftershock zones of large shallow earthquakes: Fault dimensions, aftershock area expansion, and scaling relations. *Geophys. J. Int.* **2001**, *147*, 272–293. [CrossRef]

27. Hartzell, S. Comparison of seismic waveform inversion results for the rupture history of a finite fault: Application to the 1986 North Palm Springs, California, earthquake. *J. Geophys. Res.* **1989**, *94*, 7515–7534. [CrossRef]
28. Beresnev, I.A. Uncertainties in finite-fault slip inversions: To what extent to believe? (A critical review). *Bull. Seismol. Soc. Am.* **2003**, *93*, 2445–2458. [CrossRef]
29. Hayes, G.P. Thefinite, kinematic rupture properties of great-sized earthquakes since 1990. *Earth Planet. Sci. Lett.* **2017**, *468*, 94–100. [CrossRef]
30. Goda, K.; Shoaeifar, P. Prospective Fault Displacement Hazard Assessment for Leech River Valley Fault Using Stochastic Source Modelling and Okada Fault Displacement Equations. *GeoHazards* **2022**, *3*, 277–293. [CrossRef]
31. Ozacar, A.A.; Beck, S.L.; Christensen, D.H. Source process of the 3 November 2002 Denali fault earthquake (central Alaska) from teleseismic observations. *Geophys. Res. Lett.* **2003**, *30*, 1638. [CrossRef]
32. Frankel, A. Rupture process of the M 7.9 Denali Fault, Alaska, earthquake: Subevents, directivity, and scaling of high-frequency ground motions. *Bull. Seismol. Soc. Am.* **2004**, *94*, S234–S255. [CrossRef]
33. Lu, Z.; Wright, T.J.; Wicks, C. Deformation of the 2002 Denali fault earthquakes, Alaska, mapped by Radarsat-1 interferometry. *EOS* **2003**, *84*, 425–431. [CrossRef]
34. Wright, T.; Lu, Z.; Wicks, C. Constraining the Slip Distribution and Fault Geometry of the Mw 7.9, November 3, 2002, Denali Fault Earthquake with Interferometric Synthetic Aperture Radar and Global Positioning System Data. *Bull. Seismol. Soc. Am.* **2004**, *94*, 175–189. [CrossRef]
35. Dreger, D.S.; Oglesby, D.D.; Harris, R.; Ratchkovski, N.; Hansen, R. Kinematic and dynamic rupture models of the November 3, 2002 Mw7.9 Denali, Alaska, earthquake. *Geophys. Res. Lett.* **2004**, *31*, L04605. [CrossRef]
36. Oglesby, D.D.; Dreger, D.S.; Harris, R.A.; Ratchkovski, N.; Hansen, R. Inverse kinematic and forward dynamic models of the 2002 Denali Fault earthquake, Alaska. *Bull. Seismol. Soc. Am.* **2004**, *94*, S214–S233. [CrossRef]
37. Asano, K.; Iwata, T.; Irikura, K. Estimation of Source Rupture Process and Strong Ground Motion Simulation of the 2002 Denali, Alaska, Earthquake. *Bull. Seismol. Soc. Am.* **2005**, *95*, 1701–1715. [CrossRef]
38. Hreinsdóttir, S.; Freymueller, J.T.; Fletcher, H.J.; Larsen, C.F.; Bürgmann, R. Co-seismic slip distribution of the 2002 Mw7.9 Denali Fault earthquake, Alaska, determined from GPS measurements. *Geophys. Res. Lett.* **2003**, *30*, 1670. [CrossRef]
39. Hreinsdóttir, S.; Freymueller, J.T.; Bürgmann, R.; Mitchell, J. Co-seismic deformation of the 2002 Denali Fault earthquake: Insights from GPS measurements. *J. Geophys. Res.* **2006**, *111*, B03308. [CrossRef]
40. Fabris, M.; Battaglia, M.; Chen, X.; Menin, A.; Monego, M.; Floris, M. An Integrated InSAR and GNSS Approach to Monitor Land Subsidence in the Po River Delta (Italy). *Remote Sens.* **2022**, *14*, 5578. [CrossRef]
41. Sorensen, S.P.; Meyer, K.J.; Carson, P.A.; Hall, W.J. Response of the Above-Ground Trans-Alaska Pipeline to the Magnitude 7.9 Denalli Fault Earthquake. In Proceedings of the 6th U.S. Conference and Workshop on Lifeline Earthquake Engineering, ASCE, Long Beach, CA, USA, 10–13 August 2003.
42. Eberhart-Phillips, D.; Haeussler, P.J.; Freymueller, J.T.; Frankel, A.D.; Rubin, C.M.; Craw, P.; Ratchkovski, N.A.; Anderson, G.; Carver, G.A.; Crone, A.J.; et al. The 2002 Denali fault earthquake, Alaska: A large magnitude, slip-partitioned event. *Science* **2003**, *300*, 1113–1118. [CrossRef]
43. Lanphere, M.A. Displacement history of the Denali fault system, Alaska and Canada. *Can. J. Earth Sci.* **1978**, *15*, 817–822. [CrossRef]
44. Haeussler, P.J.; Schwartz, D.P.; Dawson, T.E.; Stenner, H.D.; Lienkaemper, J.J.; Sherrod, B. Surface rupture and slip distribution of the Denali and Totschunda faults in the 3 November 2002 M 7.9 earthquake, Alaska. *Bull. Seismol. Soc. Am.* **2004**, *94*, S23–S52. [CrossRef]
45. Haeussler, P.J. Surface Rupture Map of the 2002 M7.9 Denali Fault Earthquake, Alaska; Digital Data: U.S. Geological Survey Data Series 2009, 422. Available online: http://pubs.usgs.gov/ds/422/ (accessed on 17 October 2023).
46. Fletcher, H.J. Tectonics of Interior Alaska from GPS Measure-Ments. Ph.D. Thesis, University of Alaska Fairbanks, Fairbanks, AK, USA, 2002.
47. Parashar, S.; Langham, E.; McNally, J.; Ahmed, S. RADARSAT mission requirements and concept. *Can. J. Remote Sens.* **1993**, *19*, 280–288. [CrossRef]
48. Hu, J.; Li, Z.W.; Ding, X.L.; Zhu, J.J.; Zhang, L.; Sun, Q. 3D coseismic displacement of 2010 Darfield, New Zealand earthquake estimated from multi-aperture InSAR and D-InSAR measurements. *J. Geod.* **2012**, *86*, 1–13. [CrossRef]
49. Okada, Y. Surface deformation due to shear and tensile faults in a half-space. *Bull. Seismol. Soc. Am.* **1985**, *75*, 1135–1154. [CrossRef]
50. Goda, K.; Yasuda, T.; Mori, N.; Maruyama, T. New Scaling Relationships of Earthquake Source Parameters for Stochastic Tsunami. *Coast. Eng. J.* **2016**, *58*, 1650010–1650011. [CrossRef]
51. Mai, P.M.; Beroza, G.C. A spatial random field model to characterize complexity in earthquake slip. *J. Geophys. Res.* **2002**, *107*, ESE-10. [CrossRef]

52. Goda, K.; Mai, P.M.; Yasuda, T.; Mori, N. Sensitivity of tsunami wave profiles and inundation simulations to earthquake slip and fault geometry for the 2011 Tohoku earthquake. *Earth Planets Space* **2014**, *66*, 105. [CrossRef]
53. Beauducel, F. Okada: Surface Deformation Due to a Finite Rectangular Source. MATLAB Central File Exchange. 2024. Available online: https://www.mathworks.com/matlabcentral/fileexchange/25982-okada-surface-deformation-due-to-a-finite-rectangular-source (accessed on 27 September 2024).